Bidirectional Isolated Hexamode DC–DC Converter

Vadim Sidorov, *Student Member, IEEE*, Andrii Chub, *Senior Member, IEEE*, and Dmitri Vinnikov, *Senior Member, IEEE*

***Abstract*—The proposed isolated buck–boost series resonant dc–dc converter contains two full-bridge hybrid switching cells capable of half-bridge operation. This feature is regarded as topology morphing control. Voltage buck regulation requires special modulations applied to the primary-side hybrid switching cell. In contrast, voltage boost regulation requires special modulations for the secondary-side hybrid switching cell. Combining the topology morphing control with the buck–boost regulation capability, a novel dc–dc converter operating in six different modes was derived. Moreover, the converter is capable of bidirectional operation. This article describes the influence of the topology morphing control on the dc voltage gain of the converter, which results in three boost and three buck modes. The six modes are described, and equations for the converter's dc voltage gain are provided. Based on the selected design guidelines for the power part and the control system, a 350-W prototype was designed and built. Experimental results confirm the theoretical expressions for the converter's dc voltage gain. Experimental efficiency is provided in a wide input voltage range for both energy transfer directions. Operating points with the highest thermal stress of components are analyzed with corresponding power loss breakdown calculations, confirming the measured thermal results.**

***Index Terms*—Bidirectional power flow, DC-DC power converters, microgrids, series-resonant converters, topology morphing control.**

I. Introduction

THE proliferation of dc distribution is anticipated in energy-efficient buildings in the near future [1]. Considering the dc nature of renewable energy sources and battery storage, high step-up dc–dc converters have been extensively studied in the last decade [2]. Numerous topologies, both nonisolated and isolated, were proposed. The isolated dc–dc converters could be considered a preferable solution for residential applications since the isolation barrier serves as an extra safety measure [4].

Recent studies have focused on isolated dc–dc converters with a wide input voltage range to accommodate the demands of emerging applications, such as parallel photovoltaic (PV) power optimizers, modular battery energy storage, and chargers for electric vehicles. Isolated buck–boost converters show the most promising performance in the distributed energy generation [5], [6]. They could be implemented using either one advanced switching cell, like quasi-Z-source [7], or two switching cells [8]. Among the latter type, series resonant buck–boost converters with the low quality factor of the resonant tank are justified as suitable solutions for numerous applications [9]. They are characterized by simple implementation, constant switching frequency, soft-switching, and a wide input voltage range [10].

Initially, series resonant topologies are buck converters by their nature, which can be controlled at the fixed switching frequency if their quality factor is below unity for all operating conditions [11]. By adding a secondary-side semiactive or active switching cell, it can achieve a voltage boost functionality [12]. This cell short-circuits the resonant inductor or the resonant tank to increase the energy stored, like in the conventional boost converter. The transition point between the two modes is tuned for the nominal input and output voltage.

Recent literature mainly describes the application of different voltage boosting cells at the secondary side of the series resonant converters (SRCs) to extend their regulation range. All of those cells are based on the concepts of active and semiactive rectifiers used in ac–dc applications. One of the first and simplest approaches is to short-circuit the resonant inductor by a four-quadrant switch while feeding the transformer secondary winding with voltage [8]. Even though this approach attracted significant interest [13]–[16], it suffers from the input voltage regulation range that is limited at high step-up ratios and load currents [17]. Boosting cells that short-circuit the entire resonant tank provide better voltage regulation capabilities, but higher losses in semiconductors.

In high step-up applications, the use of the half-bridge, i.e., the voltage doubler rectifier, could be recommended. There are two known implementations: with two switches and balanced current stress of the resonant tank [12] and with one switch resulting in higher efficiency but increased current stress of the resonant tank components [18]. Nevertheless, an SRC-based buck–boost converter with a full-bridge semiactive rectifier demonstrated high performance in [19]. On the other hand, its light-load efficiency was reduced compared to the converter with the half-bridge rectifier (HBR) due to the extra losses in a higher number of components and a transformer with a twice higher turns ratio.

The main drawback of the SRC-based isolated buck–boost dc–dc converters is that their performance deteriorates when the

Manuscript received December 8, 2021; revised March 7, 2022; accepted April 19, 2022. Date of publication April 26, 2022; date of current version June 24, 2022. This work was supported in part by Estonian Research Council under Grant PRG1086 and in part by the Estonian Centre of Excellence in Zero Energy and Resource Efficient Smart Buildings and Districts, ZEBE, Grant 2014-2020.4.01.15-0016 funded by the European Regional Development Fund. Recommended for publication by Associate Editor B. Chen. *(Corresponding author: Vadim Sidorov.)*

The authors are with the Department of Electrical Engineering and Mechatronics, Tallinn University of Technology, 19086 Tallinn, Estonia (e-mail: vadim.sidorov@taltech.ee; andrii.chub@taltech.ee; dmitri.vinnikov@taltech.ee).

Color versions of one or more figures in this article are available at https://doi.org/10.1109/TPEL.2022.3170229.

Digital Object Identifier 10.1109/TPEL.2022.3170229

voltage boost or buck ratio is increased. As a result, efficiency at the maximum or minimum input voltage is much lower than at the nominal voltage with no voltage boost or buck. The latter operating point could be regarded as the pass-through or dc transformer (DCX) mode that provides the highest possible efficiency for the given arrangement of the primary-side inverter and secondary-side rectifier. The topology morphing control (TMC) can make use of these DCX modes and provide a more balanced converter performance across a wide input voltage range [10]. It can be done by reconfiguring one switching cell into another, like full-bridge to half-bridge.

Recently, several attempts were made to apply the TMC to the SRC-based buck–boost dc–dc converters. However, they considered only limited cases of TMC. For example, in [20], the secondary-side boosting switching cell was reconfigured between asymmetrical full-bridge and asymmetrical half-bridge. This provided a sizable extension of the high efficiency range. However, it was proposed for a low step-up converter, whereas it is known from [21] that the asymmetrical full-bridge boost rectifier provides relatively poor performance in high step-up applications. Second, in [22], the primary-side switching cell changed its operation by changing modulation to extend the high efficiency range. Third, the primary-side full-bridge was reconfigured into the half-bridge in [22], which improved efficiency but resulted in a significant efficiency step change, compromising the converter's long-term reliability.

Another but less obvious advantage of the TMC application in the given converters is avoiding abnormal operation conditions when the voltage of the resonant capacitor(s) exceeds a certain limit, and a converter could suffer from high circulating currents [24]. This could happen at high-voltage boosting factors, whereas in TMC applications, this factor should not exceed twofold [10].

This article aims to demonstrate the full power of the TMC in an application of the SRC-based buck–boost converter by utilizing the hybrid switching cell capable of operating with different modulations on both converter's sides. Section II presents the proposed converter that features six operating modes, three buck and three boost modes, along with the analysis of the converter's operation. Section III deals with the selected design guidelines for the power part and control system. Our experimental results are given in Section IV. Finally, Section V concludes the article.

II. Bidirectional Isolation Hexamode DC–DC Converter

The topology of the proposed isolated hexamode bidirectional dc–dc converter (IHMC) consists of two versatile hybrid switching cells and a step-up isolation transformer (see Fig. 1). The topology is symmetrical; therefore, the IHMC can operate in two power flow directions. Blocking capacitors are included in the hybrid switching cells that allow for morphing the hybrid switching cells from full-bridge to half-bridge by turning ON one switch and turning OFF the other one in one leg, as shown in Fig. 2. Topology morphing in each switching cell causes a change in the dc voltage gain G of the converter. Therefore, the

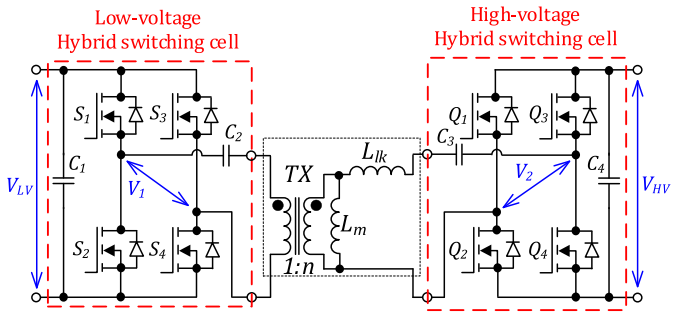

Fig. 1. Proposed isolated bidirectional hexamode dc–dc converter.

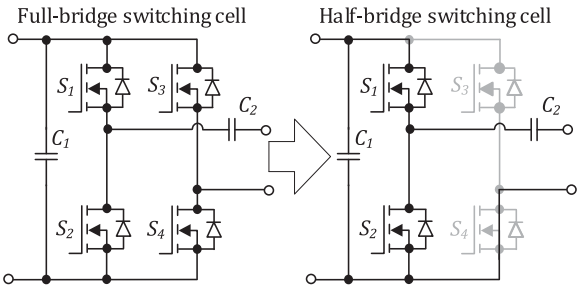

Fig. 2. Reconfiguration of the hybrid switching cell.

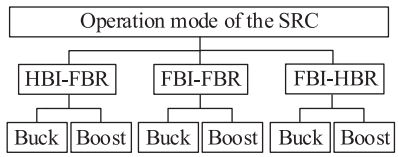

Fig. 3. Operation modes of the proposed hexamode SRC.

converter can operate in three configurations based on combinations of the full-bridge inverter (FBI) or the half-bridge inverter (HBI) at the input side, and the full-bridge rectifier (FBR) or HBR at the output side can be used to extend the input voltage range (see Fig. 3). At the same time, the switching cells allow for applying different buck and boost control methods. The combination HBI–HBR is not used in the proposed converter because the gain is the same as in the FBI–FBR, but it suffers from doubling the current stress.

In addition, the blocking capacitors neutralize any dc bias current in the isolation transformer windings, which allows for applying different asymmetrical control methods [9]. Besides, the blocking capacitors and leakage inductance of the transformer form the equivalent series resonant tank along with the transformer's leakage inductance and the series capacitors.

Hence, the angular resonant frequency is defined as follows:

$$\omega_r = \sqrt{\frac{C_3 n^2 + C_2}{L_{\rm lk} C_2 C_3}} \tag{1}$$

where $L_{\rm lk}$ is the leakage inductance of the transformer and n is the turns ratio of the transformer.

This topology is considered to operate in the discontinuous resonant current mode, i.e., with the resonant tank quality factor much below unity. Hence, the switching frequency should be

5%–10% lower than the resonant frequency to implement sufficient dead-time for soft-switching employing the transformer magnetizing current [10].

Different buck and boost control methods have been demonstrated for controlling the gain in SRCs [9], [10]. Among others, the hybrid phase-shift modulation (HPSM) and the asymmetrical pulsewidth modulation (APWM) can be highlighted as the high-efficiency buck control methods for FBI and HBI configurations, respectively. Among the boost control methods, the PSM and the APWM are the methods that perform best for both FBR and HBR configurations, respectively. The same control modes can be applied for the backward as well as for the forward power flow directions.

The normalized dc voltage gain of the IHMC for the forward power flow can be defined as follows:

$$G = \frac{V_{\rm HV}}{V_{\rm LV} \cdot n} \tag{2}$$

and for the backward power flow, the voltage gain equals

$$G = \frac{V_{\rm LV} \cdot n}{V_{\rm HV}}. \tag{3}$$

The operation modes for the forward power flow described below are grouped into boost and buck, as this converter is still essentially a buck–boost converter with three configurations.

A. Buck Control Modes

In the HPSM, the voltage gain is controlled by the phase-shift duty cycle $D_{\rm bk}$ between the leading-leg switches (S_1 and S_2) and the lagging-leg switches (S_3 and S_4), as shown in Fig. 4(b) and (c). To avoid parasitic oscillations and maintain magnetizing current circulation on the primary side, the conduction times of switches S_1 and S_2 are decreased. Switches Q_1–Q_4 operate as synchronous rectifiers. At the beginning of each half-period, one pair of switches, either Q_1 and Q_3 or Q_2 and Q_4, is turned ON, increasing the current that circulates through respective switches. When the current is decreased to zero, the rectifier switches are turned OFF. However, in the FBI–HBR mode, switch Q_1 is turned OFF continuously, whereas Q_2 is turned ON. And only two switches, Q_3 and Q_4, operate as synchronous rectifiers. As a result, the median voltage $V_{\rm med(C3)}$ of the secondary-side blocking capacitor equals $V_{\rm HV}/2$ [see Fig. 4(c)], whereas in the FBI-FBR mode, the median voltage $V_{\rm med(C3)}$ equals zero [see Fig. 4(b)]. The median voltage is used here as the average value is different from it due to the asymmetric operation of each switching cell. In both buck modes, all transistors are turned ON at zero current, and only two transistors (S_3 and S_4) are turned OFF at a high switching current.

The normalized dc voltage gain of the IHMC for the voltage buck control and the FBI–FBR configuration presented in [25] equals

$$G = B\,(\,0.25 - A) + \sqrt{B^2(\,A - 0.25)^2 + 2\,AB}. \tag{4}$$

There are two parameters used to simplify it

$$A = C_r R f_{\rm SW} \tag{5}$$

$$B = 1 - \cos(\omega_r D T_{\rm SW}) \tag{6}$$

where R is the equivalent resistance of the load, $T_{\rm SW}$ is the switching period, $f_{\rm SW}$ is the switching frequency, and D is the control duty cycle, either buck or boost. In addition, an equation for the duty cycle can be defined as follows:

$$D_{\rm bk} = \frac{1}{\omega_r \cdot T_{\rm SW}} \arccos\left(1 - \frac{G^2}{2 \cdot A - G \cdot (A - 0.25)}\right). \tag{7}$$

The equations of the voltage gain and the duty cycle are based on the assumption of lossless components of the converter.

In the case of the buck FBI–HBR mode, an equation for the gain was presented in [23] in the following form:

$$G = \frac{1}{2}\left(B\,(\,1 - A) + \sqrt{B^2(\,A - 1)^2 + 8\,AB}\right). \tag{8}$$

The duty cycle presented in [23] can be rewritten as follows:

$$D_{\rm bk} = \frac{1}{\omega_r \cdot T_{\rm SW}} \arccos\left(1 - \frac{G^2}{2 \cdot A - G \cdot (A - 1)}\right). \tag{9}$$

The APWM is applied to control the voltage buck gain in the HBI–FBR configuration. In this mode, switch S_3 is turned OFF, and switch S_4 is turned ON continuously. The control signals of switches S_1 and S_2 are complementary, separated by the dead-times, and asymmetrical [see Fig. 4(a)]. The control signal of switch S_1 equals the duty cycle $D_{\rm bk}$. The condition time of switch S_2 is decreased, as in previous modes, and provides sufficient time for a complete sinusoidal half-wave of the resonant current. This improves the soft-switching performance of the converter. Only transistor S_1 is turned OFF at a high switching current in this mode.

The normalized dc voltage gain of the SRC for the APWM control method in the HBI–FBR configuration equals [23]

$$G = 0.5\left(B\,(\,0.5 - A) + \sqrt{(\,B\,(\,A - 1))^2 + 4\,AB}\right). \tag{10}$$

An equation for the duty cycle can be written as follows:

$$D_{\rm bk} = \frac{1}{\omega_r \cdot T_{\rm SW}} \arccos\left(1 - \frac{G^2}{A - G \cdot (A - 0.5)}\right). \tag{11}$$

B. Boost Control Modes

The phase-shift boost modulation is used in the FBI–FBR and HBI–FBR configurations [see Fig. 4(d) and (e)]. In the FBI–FBR configuration, the primary-side switches (S_1–S_4) are controlled complementarily in two diagonals. The median voltages of the blocking capacitors C_2 and C_3 equal zero. In the HBI–FBR configuration, switch S_4 is turned ON continuously, whereas the other, S_3, is turned OFF. The median voltage $V_{\rm med(C2)}$ of the input-side capacitor C_2 equals $V_{\rm LV}/2$. In both configurations, the control signals of the switches (Q_3 and Q_4) are complementary and shifted by the duty cycle $D_{\rm bt}$ relative to the control signals of the inverter switches (S_1–S_4). This modulation shorts the output side of the resonant tank and charges energy into it. The other switches (Q_1 and Q_2) operate as the synchronous rectifier. They are turned ON softly and turned OFF at a high switching current, whereas other transistors are switched at zero current.

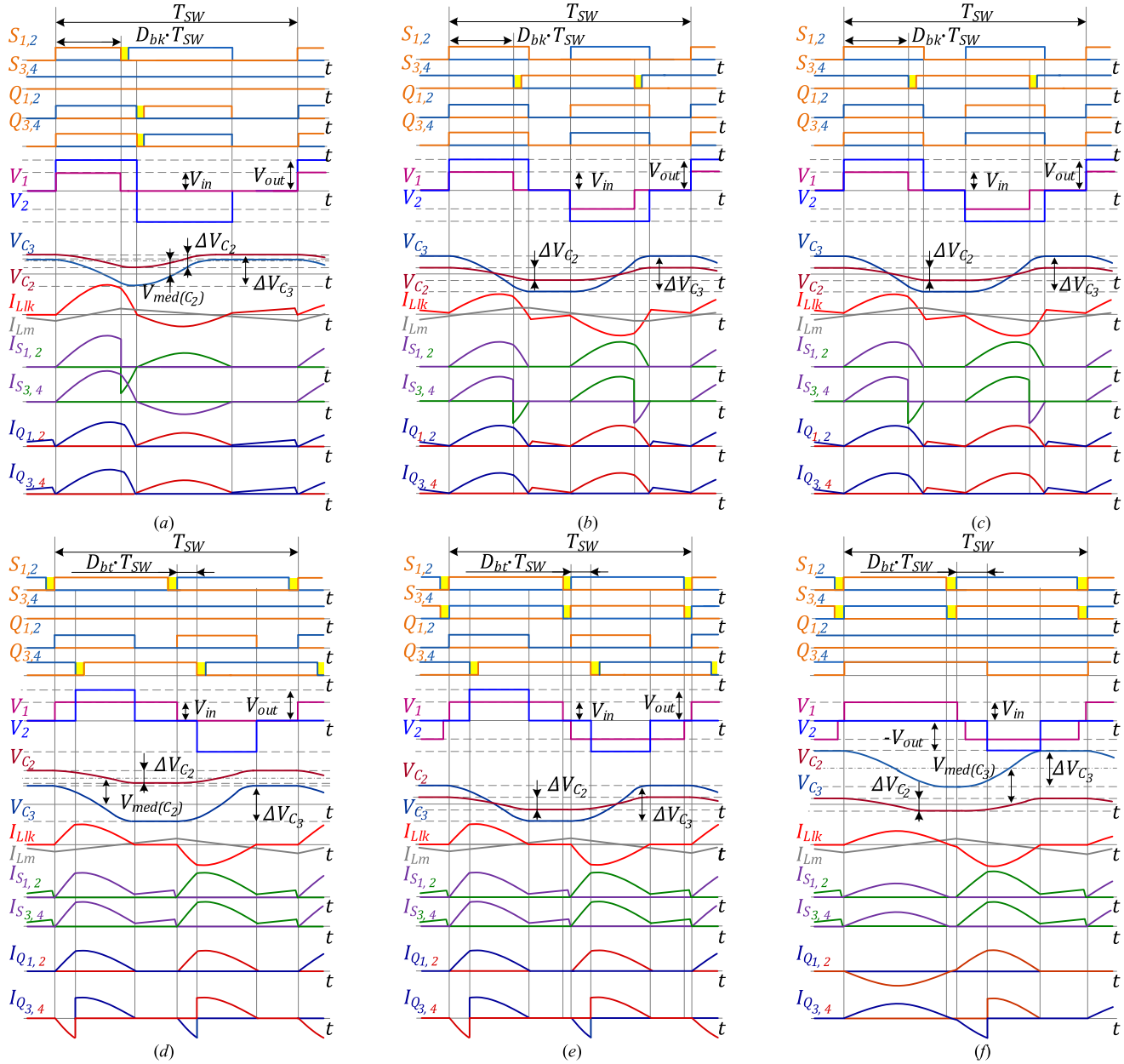

Fig. 4. IBMC operation in the buck mode for three configurations: HBI–FBR (a), FBI–FBR (b), and FBI–HBR (c). IBMC operation in the boost mode for three configurations: HBI–FBR (d), FBI–FBR (e), and FBI–HBR (f).

The gain for the boost mode and the FBI–FBR configuration presented in [25] equals

$$G = \frac{1}{2-B}\left(1+\sqrt{1+4\,A\cdot B\cdot(2-B)}\right). \tag{12}$$

From (12), the duty cycle could be obtained as follows:

$$D_{\text{bt}} = \frac{1}{\omega_r \cdot T_{\text{SW}}}\arccos\left(1-\frac{G^2-G}{0.5\cdot G^2+2\cdot A\cdot G}\right). \tag{13}$$

In the HBI–FBR configuration, the gain in the boost mode is given as follows [25]:

$$G = \frac{1}{2-B}\left(\frac{1}{2}+\sqrt{\frac{1}{4}+A\cdot B\cdot(2-B)}\right). \tag{14}$$

And the duty cycle of the boost HBI–FBR mode is given as follows:

$$D_{\text{bt}} = \frac{1}{\omega_r \cdot T_{\text{SW}}}\arccos\left(1-\frac{2G^2-G}{G^2+A\cdot G}\right). \tag{15}$$

In the case of the FBI–HBR configuration, the asymmetrical PWM voltage boost is applied for controlling the converter gain [see Fig. 4(f)]. In this mode, the output-side switch Q_1 is

TABLE I
SEQUENCE OF OPERATION MODES

$\frac{V_{HV}}{V_{LV}\cdot n}$	Modulation	
	Forward	Backward
0–0.5	Buck HBI-FBR (Fig 4a)	Boost FBI-HBR (Fig 4f)
0.5–1	Boost HBI-FBR (Fig 4d) Buck FBI-FBI (Fig 4b)	Buck FBI-HBR (Fig 4c) Boost FBI-FBR (Fig 4e)
1–2	Boost FBI-FBR (Fig 4e) Buck FBI-HBR (Fig 4c)	Buck FBI-FBR (Fig 4b) Boost HBI-FBR (Fig 4d)
2 >	Boost FBI-HBI (Fig 4f)	Buck HBI-FBR (Fig 4a)

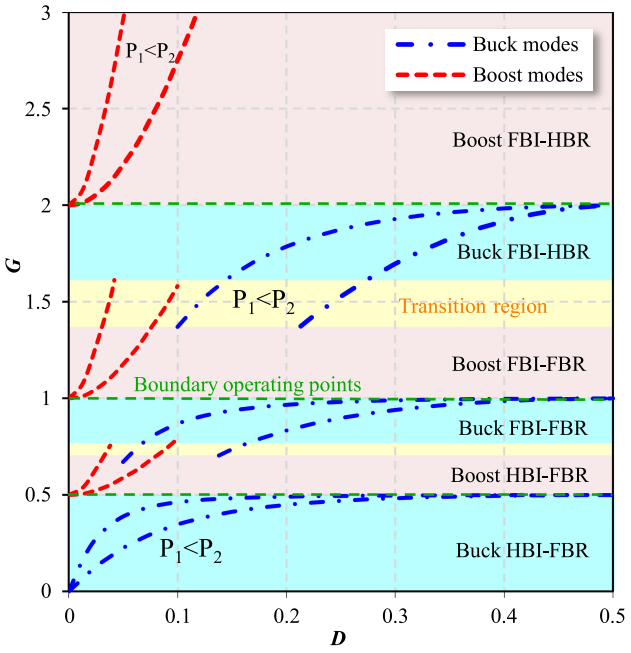

Fig. 5. Normalized voltage gain characteristics for the IHMC.

turned OFF continuously, whereas Q_2 is turned ON. The energy is charged in the resonant tank by extending the conduction time of the switch Q_4 by the duty cycle $D_{\rm bt}$. At the same time, switch Q_3 operates as the synchronous rectifier. In the first-half period, the resonant current is always sinusoidal. It should be noted that the duty cycle of switches S_1 and S_4 is decreased from 0.5 to D_p for achieving zero current switchings.

Therefore, the duty cycle of switches S_2 and S_3 equals $(1 - D_p)$. In this mode, only switch Q_4 is turned OFF at a high switching current.

For the FBI–HBR configuration, the gain in the boost mode equals [26]

$$G = \frac{1}{1-0.5B}\left(1+\sqrt{1+4\,A\cdot B\cdot(1-0.5B)}\right). \quad (16)$$

The corresponding duty cycle is given as follows [26]:

$$D_{\rm bt} = \frac{1}{\omega_r \cdot T_{\rm SW}} \arccos\left(1-\frac{G^2-2G}{0.5\cdot G^2+4\cdot A}\right). \quad (17)$$

C. Normalized Voltage Gain

Each control method can be applied in the forward power direction as well as in the backward direction. Table I shows the sequences of operation modes for both directions with respect to the voltage ratio between the high- and low-voltage ports.

The normalized voltage gain of the IHMC in any direction is plotted in Fig. 5 as the function of the generalized control duty cycle D for two values of the operating powers P_1 and P_2 using (4), (8), (10), (12), (14), and (16). Measured voltage gain characteristics will be provided in Section IV (see Fig. 15). As described above, the converter operates under six control modes. Relative to the definition of the voltage gain (2) and (3), the sequence of operation modes is the same in both directions. The gain ranges between the boost HBI–FBR and the buck FBI–FBR modes; the boost FBI–FBR and the buck FBI–HBR modes are transition regions. Points of transitions between these modes are selected based on the experimental or estimated efficiency curves.

It should be noted that the buck control methods feature a dead control zone, where the voltage gain G depends weakly on the duty cycle. This zone is nonusable for the converter control in practice, especially at a light load.

III. Design and Control Guidelines

A. Isolation Transformer

The efficiency of the IHMC depends on the design of the isolation transformer. The first parameter of the transformer is the turns ratio n. The turns ratio is selected based on the required voltage gain range. As shown in Fig. 5, theoretically, the voltage gain range of the proposed converter can cover the range $G = 0$–3. However, for optimization of the converter's performance, the minimum duty cycle $D_{\rm bk(min)}$ in the buck HBI–FBR mode and the maximum duty cycle $D_{\rm bt(max)}$ in the boost FBI–HBR mode should be limited. The reason is that the duty cycle values close to zero in the buck mode would result in a very short conduction time of the switch S_1. At the same time, the duty cycle values close to one in the boost mode would result in very high charged energy in the resonant tank. Both cases cause a high peak and rms currents in switches and the transformer and, consequently, high switching and conduction losses in the converter. Thus, selection of the operation voltage gain range is a tradeoff between the power losses and the voltage gain range.

In summary, the turns ratio of the transformer can be calculated as follows:

$$n = \frac{V_{\rm HV(max)}}{V_{\rm LV(min)}\cdot G_{\rm max}} \quad (18)$$

where $V_{\rm HV(max)}$ is the maximum operation voltage of the high-voltage side; $V_{\rm LV(min)}$ is the minimum operation voltage of the low-voltage side; $G_{\rm max}$ is the maximum voltage gain in the boost FBI–HBR mode (16), which is calculated using $D_{\rm bt(max)}$.

The next parameter of the transformer is the flux density $B_{\rm max}$ that achieves its maximum value in the boundary operating points between the boost and the buck modes under the FBI–FBR topology in any direction. The flux density $B_{\rm max}$ in the forward and backward directions can be calculated, respectively,

as follows:

$$B_{\max(\mathrm{fw})} = \frac{V_{\mathrm{LV}}}{4 \cdot f_S \cdot A_e \cdot N_{\mathrm{pr}}} \tag{19}$$

$$B_{\max(\mathrm{bw})} = \frac{V_{\mathrm{HV}}}{4 \cdot f_S \cdot A_e \cdot N_{\mathrm{sec}}} \tag{20}$$

where A_e is the effective core area, and N_{pr} and N_{sec} are the turns numbers of the primary and secondary windings, respectively.

The following parameter is the magnetizing inductance L_m, which influences the dead-time $T_{D(\mathrm{pr}.lc)}$ between input-side switches in the boost modes directly. Moreover, the longest dead-time is required in the boost HBI–FBR mode. Therefore, the maximum value of the magnetizing inductance for the forward direction can be defined as follows:

$$L_{m(\max)} \leq \frac{T_{D(\mathrm{in}.lc)} \cdot n}{16 \cdot f_S \cdot C_{\mathrm{oss(LV)}}} \tag{21}$$

where $C_{\mathrm{oss(LV)}}$ is the parasitic output capacitance of one low-voltage switch.

In the backward direction, the maximum value of the magnetizing inductance can be calculated as follows:

$$L_{m(\max)} = \frac{T_{D(\mathrm{in.bt})}}{16 \cdot f_S \cdot C_{\mathrm{oss(HV)}}} \tag{22}$$

where $C_{\mathrm{oss(HV)}}$ is the parasitic output capacitance of the high-voltage switches.

During the dead-time, the body diodes of switches conduct the current. It increases the conduction losses of the converter due to a high forward voltage and resistance of the body diodes. On the other hand, a low magnetizing inductance is a reason for a high magnetizing current, which circulates through the primary side in the boost modes and through the secondary side in the buck modes. As a result, it increases the conducting losses in the transformer windings and MOSFETs on both sides, as well as the switching losses of the primary-side MOSFETs. Therefore, there is a balance between the minimum dead-time and power losses from the magnetizing current.

Previous analysis [9] shows that the inductance of the resonant tank L_r should be as large as possible for achieving the lowest amplitude of the resonant current and, as a result, the lowest conduction and switching losses in the converter. On the other hand, the maximum value of the leakage inductance is limited by the input voltage range and the maximum power. The maximum value can be defined in the buck FBI–HBR mode as follows:

$$L_r < \frac{V_{\mathrm{out}} \cdot f_S}{I_{\mathrm{out}} \cdot {\omega_r}^2}. \tag{23}$$

To achieve a high resonant inductance value, an external inductor is usually added in series with the isolation transformer. However, an approach used for the transformer design based on the hybrid split bobbin was described in [27]. It allows for increasing and adjusting the leakage inductance and, consequently, avoiding an external inductor.

Finally, it is important to consider the winding resistance in the design of the transformer. Since the spectrum of the resonance current in each mode includes a set of odd harmonics, the wires of windings should have low resistance at harmonics up to 11 and reduce the skin and proximity effects. The best solution is to use the Litz wires with the lowest diameter strands (0.04 mm in the given case).

B. Series Blocking Capacitors

Considering the ac voltage across the blocking/resonant capacitors, only a few types of capacitors can be selected for operation in the resonant tank. In practice, low-voltage high-current capacitors, such as ceramic capacitors, have a high deviation of capacitance due to changing applied voltage and operating temperature. At the same time, film capacitors can operate with high voltage and have a low deviation of capacitance but feature low capacitance density per volume. According to these aspects, the resonant frequency can be adjusted by the high-voltage film capacitors C_3. The capacitance of the low-voltage ceramic capacitors C_2 should be much more than C_3 ($C_2 >> C_3$) to avoid deviation of the resonant frequency.

The value of the capacitor C_3 can be calculated as follows:

$$C_3 \approx \frac{1}{L_{\mathrm{lk}} {\omega_r}^2}. \tag{24}$$

The maximum operating voltage of the capacitor C_3 is achieved in the forward buck FBI–HBR mode at a low duty cycle and can be defined as follows:

$$V_{C3(\max)} = \frac{V_{\mathrm{HV}} + \Delta V_{C3}}{2} \tag{25}$$

where ΔV_{C3} is the peak-to-peak voltage ripple of the capacitor C_3

$$\Delta V_{C3} = \frac{I_{\mathrm{out}}}{C_3 \cdot f_S}. \tag{26}$$

In the forward boost HBI–FBR mode, the low-voltage capacitor C_2 is under maximum voltage stress that equals

$$V_{C2(\max)} = \frac{V_{\mathrm{LV}} + \Delta V_{C2}}{2} \tag{27}$$

where ΔV_{C2} is the peak-to-peak voltage ripple of the capacitor C_2

$$\Delta V_{C2} = \frac{I_{\mathrm{in}}}{C_2 \cdot f_S \cdot n}. \tag{28}$$

C. Semiconductors

Typically, the transistors are selected based on the maximum voltage and current stresses. The maximum voltage of the low-voltage side transistors equals V_{LV}, and the maximum voltage of the high-voltage side transistors equals V_{HV}. At the current stress, switches provide different peaks and rms currents in different operation modes and power flow directions. The highest current stress of the low-voltage and high-voltage side transistors is achieved in the buck FBI–HBR mode in the backward and forward directions, respectively. Expressions for the calculation of the peak and rms currents in the buck FBI–HBR mode are derived in Appendix A.

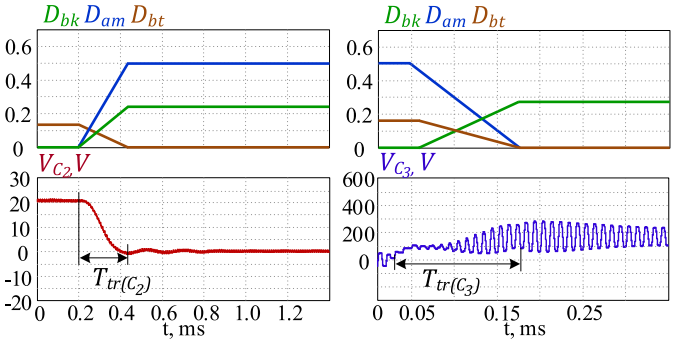

Fig. 6. Simulated soft transition (a) between HBI–FBR and FBI–FBR and (b) between FBI–FBR and FBI–HBR.

D. Converter Control

Several aspects should be taken into account in the design of a control system for the IHMC. One of the aspects is the dead-time $T_{D(hc)}$ between control signals of switches, which operate with a high switching current. The dead-time is dependent on the output capacitance, operation voltage, and current of transistors. The maximum dead-time is required at a low operating power. For the low-voltage side transistors, the minimum dead-time can be calculated as follows:

$$T_{D(\text{in}.lc)} \geq \frac{2 \cdot C_{\text{oss(LV)}} \cdot V_{\text{LV(max)}}}{I_{L\text{lk}_m(\text{min})} \cdot n} \tag{29}$$

where $I_{L\text{lk}_m(\text{min})}$is a minimum switching current.

For the high-voltage side transistors, the minimum dead-time equals

$$T_{D(\text{in}.lc)} \geq \frac{2 \cdot C_{\text{oss(HV)}} \cdot V_{HV(\text{max})}}{I_{L\text{lk(min)}}}. \tag{30}$$

The second aspect is transitions between the configurations of the topology. The series blocking capacitors feature different dc voltage stresses in different configurations. For example, for the HBI–FBR configuration, the median voltage $V_{\text{med(C2)}}$ of the input-side capacitor C_2 equals $V_{\text{LV}}/2$, but in the FBI–FBR, $V_{\text{med(C2)}}$ equals zero. It means that the capacitor must be recharged during a transition between two topology configurations. This causes high current stress in the circuit, and consequently, the power semiconductor devices can be destroyed. However, the algorithm for soft transitions between different control modes and topology configurations has been proposed in [25]. The main idea of the soft transition algorithm is in the linear increase or decrease in the duty cycles of switches S_3, S_4 or Q_1, Q_2 due to their static operation in one of the adjacent modes during the transition, as shown in Fig. 6. Fig. 7(a) and (b) shows the control signals of switches during the soft transition between HBI and FBI and between FBR and HBR, respectively. The duty cycle of the next operation mode is calculated based on the feed-forward control using (7), (9), (13), and (15). As shown in [25], voltage points for transition between control modes have to be selected based on the efficiency curves of each mode. To avoid voltage oscillation at the transition points, it is necessary to apply hysteresis in the transition algorithm.

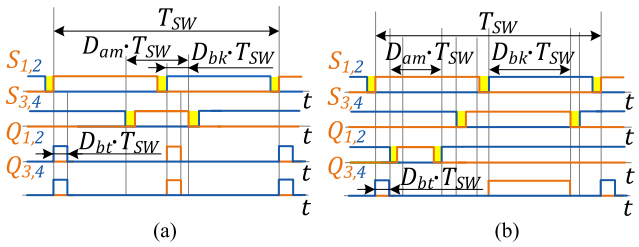

Fig. 7. Control signals of switches during the soft transition (a) between HBI and FBI and (b) between FBR and HBR.

This algorithm provides recharging of the blocking/resonant capacitors and allows for avoiding oscillations and high peaks in the currents of the converter and maintaining the input voltage at a regulated level during the transition time, which can be calculated for the transition between the FBI and the HBI as

$$T_{\text{tr}(C2)} \geq 2 \cdot \pi \cdot \frac{\sqrt{L_m \cdot C_2}}{n} \tag{31}$$

and for the transition between the FBR and the HBR, the transition time is defined as follows:

$$T_{\text{tr}(C3)} \geq 2 \cdot \pi \cdot \sqrt{L_{\text{lk}} \cdot C_3}. \tag{32}$$

A special algorithm is not required for the transition between buck and boost modes within one topology configuration, e.g., between the buck FBI–FBR and the boost FBI–FBR modes because the converter crosses the boundary operating point smoothly. The reason is that at these points, the duty cycle of buck modes of 0.5 and the duty cycle of boost modes of 0 are technically the same operating point.

Implementation of the synchronous rectifier is the third aspect of the IHMC control system. A simple approach for the realization of the synchronous rectifier control circuit is based on the measurement of current transformers and comparators, as shown in Fig. 8. Some microcontrollers, such as STM32, have internal comparators connected with PWM timers. It allows for the implementation of a compact control circuit. The comparators detect a low level of the falling resonant current and send a signal to timers for turning OFF rectifier switches.

Since the IHMC operates in two directions and the magnetizing current can circulate through the low-voltage or the high-voltage side, two control circuits on low- and high-voltage sides are used in the control system of the synchronous rectifier to neutralize the effects of the magnetizing current. It allows for correct detection of an instant when the switches should be turned OFF. Thus, the current transformer on the high-voltage side and comparators COMP3 and COMP4 are responsible for operation in the forward mode, and the current transformer on the low-voltage side and comparators COMP1 and COMP2 are responsible for operation in the backward mode. Fig. 9 presents an example of the control signal generation in the buck FBI–FBR and the boost FBI–FBR modes in the forward direction based on microcontroller timers. Based on this example, other modes in both directions can be realized. This control circuit is also used for controlling the primary switches in the buck mode. The current transformer measuring the secondary winding current should have reinforced isolation.

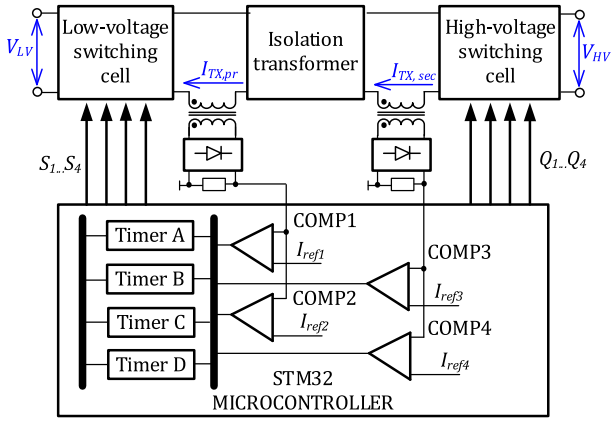

Fig. 8. Control circuit of the synchronous rectifier.

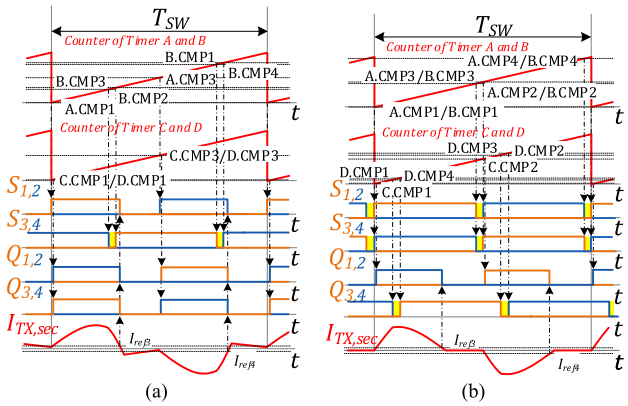

Fig. 9. Generalized principle of the control signal generation in the (a) buck FBI–FBR and (b) boost FBI–FBR modes in the forward power direction.

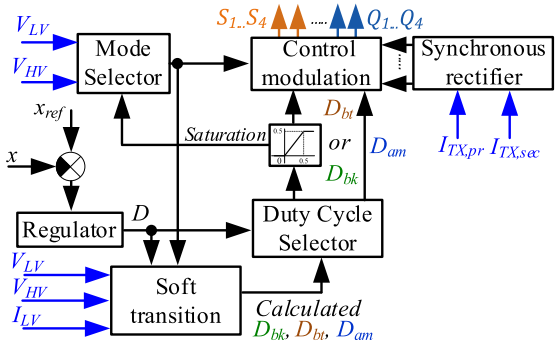

Fig. 10. Block diagram of a closed-loop control system.

In summary, the example of a closed-loop control system for the regulation of some variable x is shown in Fig. 10. The mode selector chooses a control mode automatically; therefore, the duty cycles D_{bk} and D_{bt} are based on an operation voltage gain. At the same time, when the system achieves one of the thresholds for the soft transition between the boost HBI–FBR and the buck FBI–FBR or the boost FBI–FBR and the buck FBI–FBH, the control system switches to the soft transition algorithm during the required time and operates with calculated duty cycles D_{bk}, D_{bt}, and D_{am}. This example of the control system can be used in both power directions.

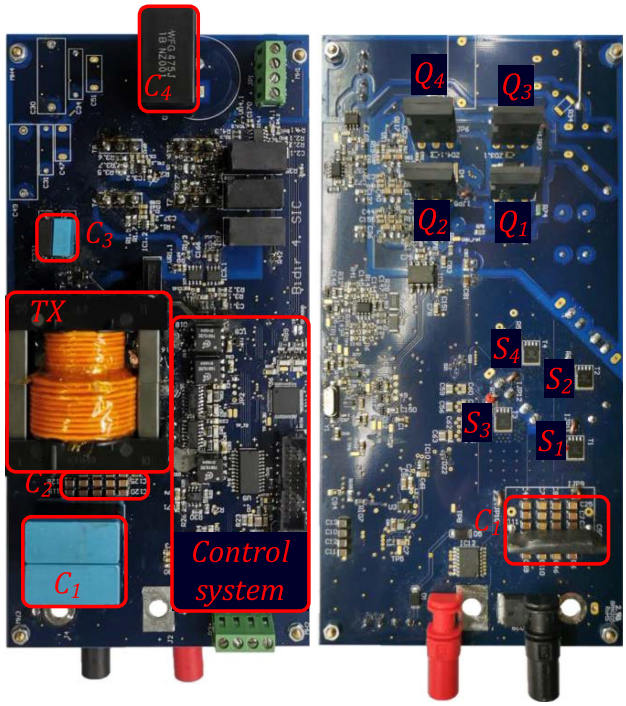

Fig. 11. Prototype of the IHMC.

TABLE II
PROTOTYPE PARAMETERS AND COMPONENTS

Operating parameters	
Low voltage, V_{LV}	10…60 V
Maximum low-voltage current, I_{LV}	12 A
High voltage, V_{HV}	350 V
Switching frequency, f_{SW}	100 kHz
Operating power range	20…350 W
Components	
S_1…S_4	On Semiconductor FDMS86180
Q_1…Q_4	LittleFuse LSIC1MO120E0080
C_1	150 µF
C_2	52 µF
C_3	25 nF
C_4	5.2 µF
L_{lk}	115 µH
L_m	1.95 mH
n	13.5

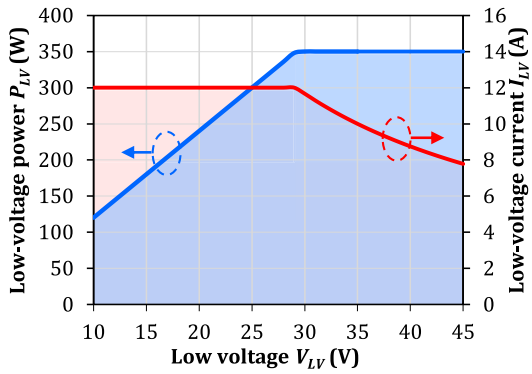

Fig. 12. Case study safe operation area for the designed IHMC prototype.

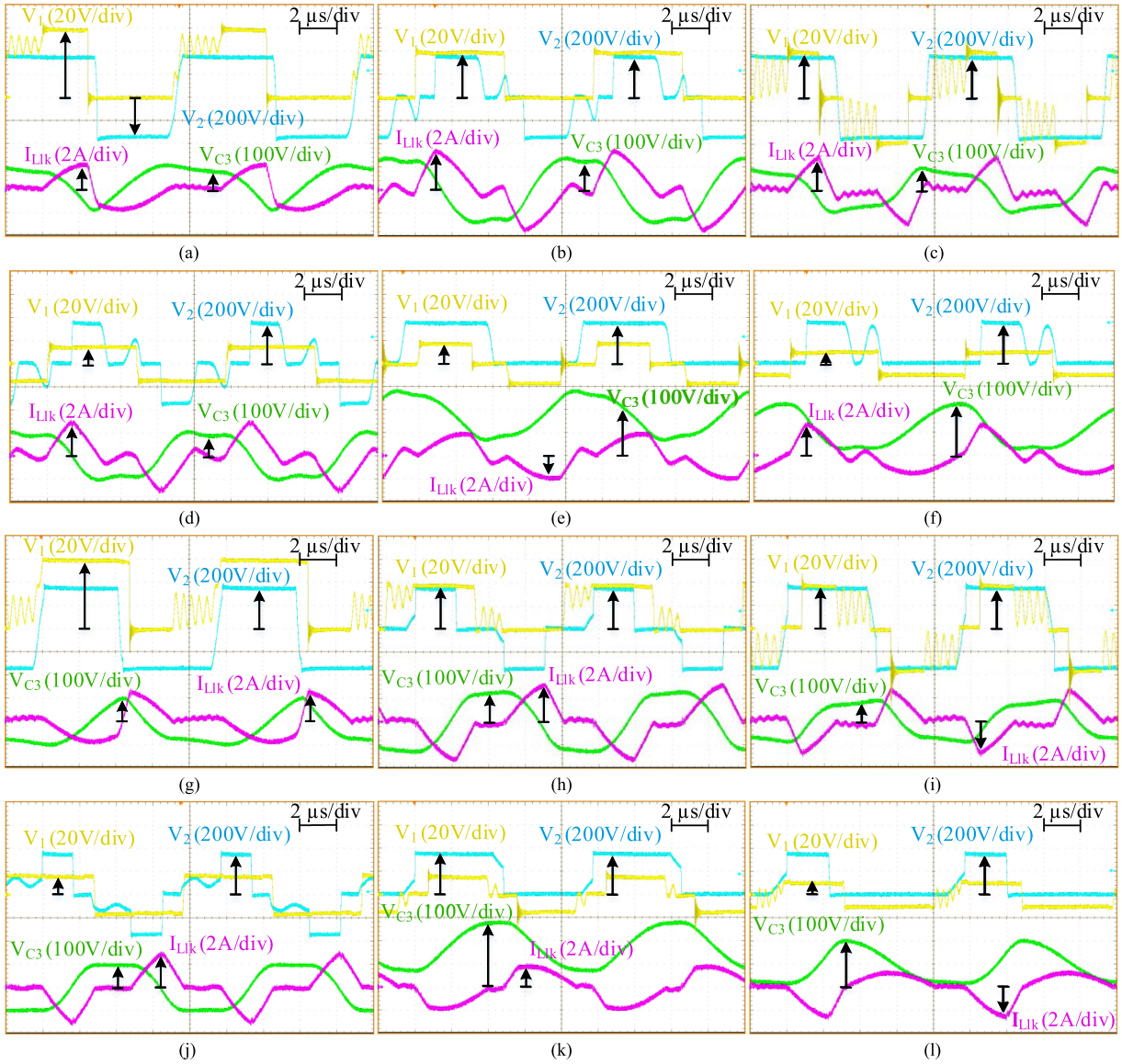

Fig. 13. Experimental steady-state waveforms of the IHMC operating in the forward mode at $V_{LV} = 60$ V and $P_{LV} = 350$ W for the buck HBI–FBR (a), at $V_{LV} = 40$ V and $P_{LV} = 350$ W for the boost HBI–FBR (b) and the buck FBI–FBR (c), at $V_{LV} = 17$ V and $P_{LV} = 205$ W for the boost FBI–FBR (d) and the buck FBI–HBR (e), and at $V_{LV} = 10$ V and $P_{LV} = 120$ W for the boost FBI–HBR (f); in the backward mode at $V_{LV} = 60$ V and $P_{LV} = 350$ W for the boost FBI–HBR (g), at $V_{LV} = 40$ V and $P_{LV} = 350$ W for the buck FBI–HBR (h) and the boost FBI–FBR (i), at $V_{LV} = 17$ V and $P_{LV} = 205$ W for the buck FBI–FBR (j) and the boost HBI–FBR (k), and at $V_{LV} = 10$ V and $P_{LV} = 120$ W for the buck HBI–FBR (l).

IV. Experimental Results

A prototype of the IHMC shown in Fig. 11 was built to validate the converter's performance in a wide voltage gain range in both power flow directions. Table II lists the main components used in the prototype. The isolation transformer was designed based on the hybrid split bobbin [27] that eliminates the need for an external inductor. It should be noted that electrolytic capacitors are not used in the prototype according to the requirements of parallel PV power optimizer applications. The following measurement equipment was used: oscilloscope Tektronix DPO7254, differential voltage probes Tektronix P5205A, current sensors Tektronix TCP0030A and PEM ultra-mini CWT015, precision power analyzer Yokogawa WT1800, and thermal camera Fluke Ti25.

The prototype was designed for operation in the safe operating area (SOA) shown in Fig. 12. The SOA covers the operation ranges of typical market-leading PV module types (60- and 72-cell silicone PV modules) and batteries (12 V, 24 V, and 48 V).

A. Steady-State Waveforms

Fig. 13 shows measured steady-state waveforms of the output voltage of the low-voltage (yellow) and high-voltage (blue) switching cells, the voltage of the high-voltage side resonant

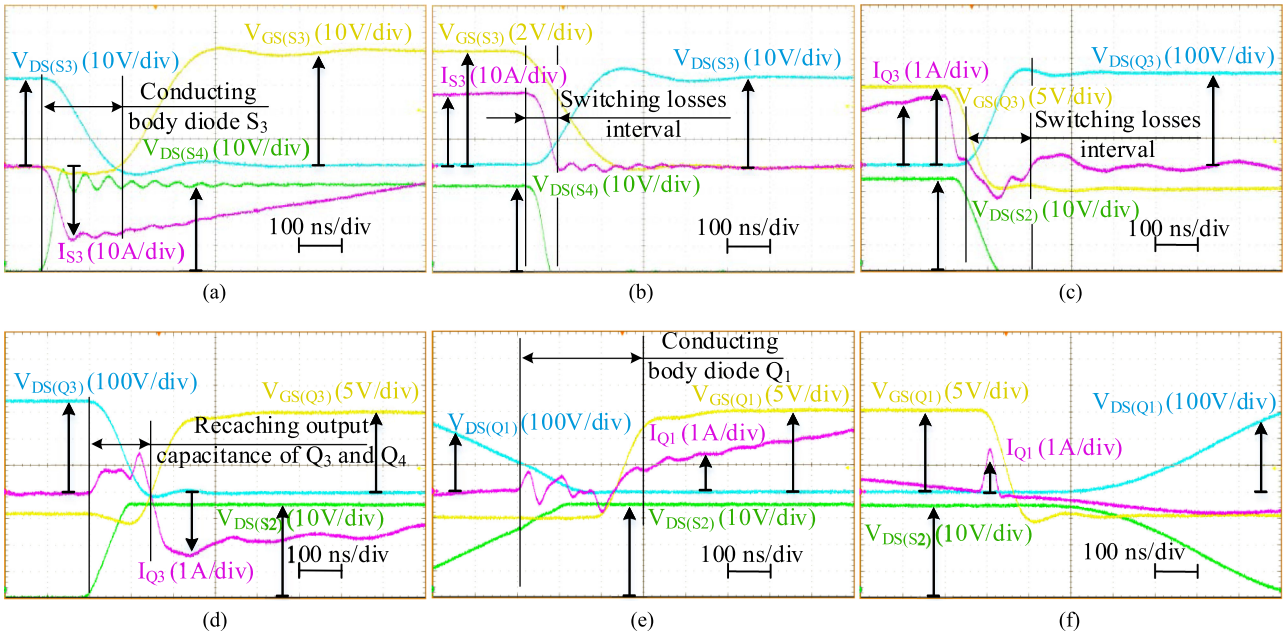

Fig. 14. Experimental switching-ON (a) and -OFF (b) waveforms of transistor S_3 at $V_{LV} = 35$ V and $P_{LV} = 250$ W under the buck FBI–FBR, switching-ON (c) and -OFF (d) waveforms of transistor Q_3, and switching-ON (e) and -OFF (f) waveforms of transistor Q_1 at $V_{LV} = 20$ V and $P_{LV} = 200$ W under the boost FBI–FBR in the forward mode.

capacitor C_3 (green), and the current of the high-voltage side transformer current (magenta) of the IHMC operating in the boundary points of each control mode. In all buck modes, the transformer current and voltage of switching cells have a parasitic oscillation between the output capacitances of the inverter transistors and the leakage inductance in the zero states. Also, boost modes feature parasitic oscillations between the output capacitances of the rectifier transistors and the leakage inductance.

In the waveforms of the transformer current, the magnetizing current circulates through the high-voltage side in the buck mode for the forward power flow and the boost mode for the backward power flow. Therefore, in other modes, the leakage inductance current circulates through the low-voltage side. The leakage inductance produces additional power losses in the convert sides; however, it allows for recharging output capacitances of transistors and achieving soft switching.

B. Varification of Soft-Switching Operation

Fig. 14 shows zoomed experimental switching-ON and -OFF waveforms of the transistor S_3 in the buck FBI–FBR mode and transistors Q_1 and Q_3 in the boost FBI–FBR mode, all in the forward mode. These are the most critical switching cases. As described above, two primary transistors S_3 and S_4 and two secondary transistors Q_3 and Q_4 are turned OFF at high switching current. The waveforms of the transistors S_3 and Q_3 show that the output capacitance of transistors in a leg is recharged by a high switching current after switching OFF one of the transistors. After that, a body diode of the next transistor conducts the current during the dead-time. Thus, the next transistor in the leg is turned ON at zero voltage.

Rectifier switches [Q_1 in Fig. 14(e) and (f)] are turned ON and OFF at zero current. During the zero-current state, output capacitances of the rectifier switches are recharged. Under the same condition, primary switches S_1 and S_2 are switched under the buck FBI–FBR and the buck FBI–HBR modes and all primary switches in the boost modes.

According to Fig. 14, it can be summarized that all transistors are turned ON at zero voltage or current. Thus, the IHMC operates without switch-ON losses, and only two transistors are switched OFF at high current.

C. Comparison of Experimental and Theoretical Control Variables

Fig. 15 shows the calculation results of the theoretical dc gain (solid lines) based on (4), (8), (10), (12), (14), and (16) in comparison with the measured gain values (markers) for all control methods in both power flow directions, while staying within the SOA. The figures show good agreement between the theoretical and experimental results for all the applied methods. Small differences between theoretical and experimental values occur outside the target regulation range and are mostly associated with the assumptions of a lossless system, neglecting the influence of the magnetizing inductance and power losses during the analysis.

D. Efficiency Evaluation

The measured efficiency of the IHMC is shown in Fig. 16 for both power flow directions, which was measured at the

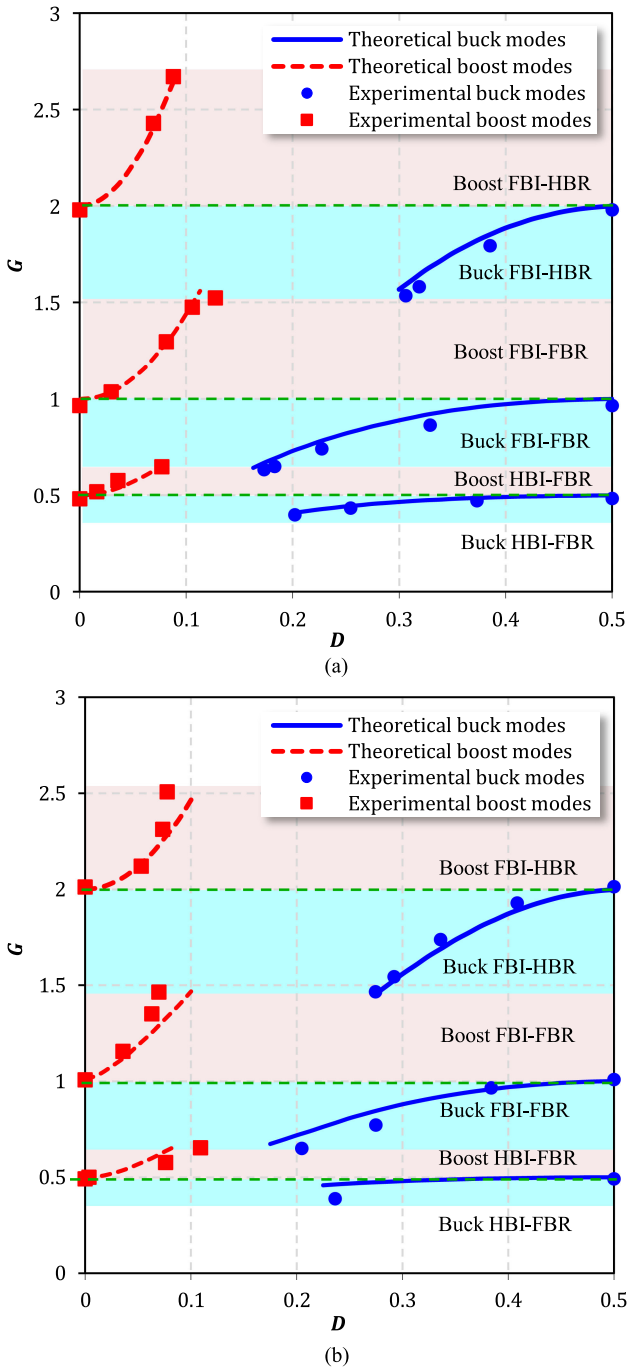

Fig. 15. Experimental and theoretical normalized voltage gain characteristics for the IHMC in the forward mode (a) and in the backward mode (b).

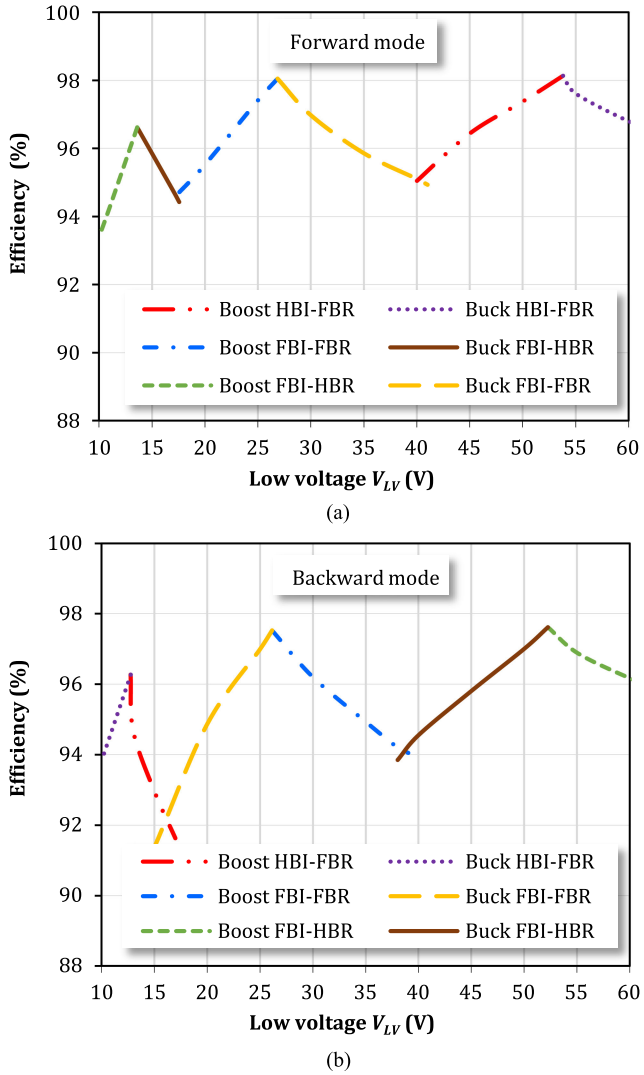

Fig. 16. Efficiency of the IHBC operating in the forward (a) and the backward (b) directions at the borders of the SOA from Fig. 12.

SOA envelope, i.e., maximum current and maximum power ranges. The converter operates with a 50% duty cycle (like a dc transformer) at $V_{\mathrm{LV}} = 13$, 26, and 52 V, where the efficiency achieves the maximum values. At this point, the transformer current is virtually sinusoidal, and as a result, all switches are soft-switched. The maximum efficiency of the IHMC is 98.1% in the forward mode and 97.6% in the backward mode at $V_{\mathrm{LV}} = 52$ V. This difference in peak efficiency results from the SOA application regarding the low-voltage side power. It means that the input power (on the high-voltage side) in the backward power flow direction is higher than the power on the low-voltage side. Another reason for the efficiency difference between power in the flow directions is the longer dead-times for the high-voltage transistors. With an increase or decrease in the input voltage from the DCX points, the converter operates in buck or boost mode, and the efficiency decreases. This is mainly associated with the increasing rms and switching currents in the converter, which results from the shortening of the active states applied to the isolation transformer. As can be seen from Fig. 16, the efficiency curves of the boost HBI–FBR and buck FBI–FBR modes are crossed at $V_{\mathrm{LV}} = 40$ V. The efficiency curves of the boost FBI–FBR and buck FBI–HBR modes are crossed at $V_{\mathrm{LV}} = 17$ V. These are the points recommended for implementing the transition between the HBI–FBR and the FBI–FBR configurations and between FBR–FBR and FBI–HBR, respectively, by using the proposed approach of the linear duty cycle ramp.

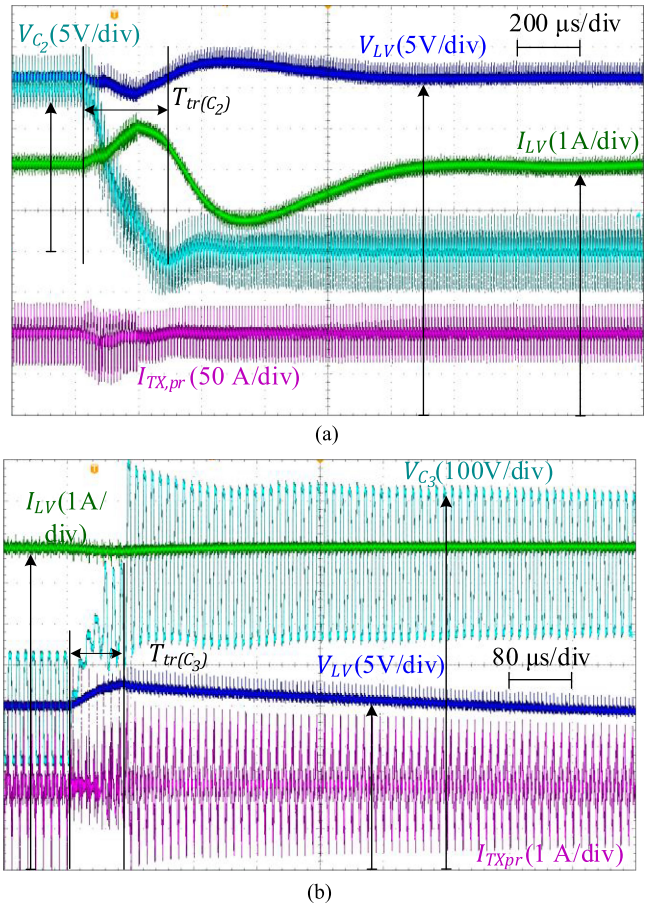

Fig. 17. Experimental waveforms of the soft transition (a) from the boost HBI–FBR to the buck FBI–FBR at $V_{\mathrm{LV}} = 40$ V and (b) from the boost FBI–FBR to the buck FBI–HBR at $V_{\mathrm{LV}} = 20$ V.

E. Verification of the Soft Mode Transitions

For verification of the described algorithm of soft transition, experimental waveforms of transitions from the boost HBI–FBR mode to the buck FBI–FBR mode and the boost FBI–FBR mode to the buck FBI–HBR mode are shown in Fig. 17. These two cases of transition between modes are the most critical due to the need of recharging capacitances in series with the transformer windings. Therefore, these cases have been selected for experimental verification. As described in Section III, other cases of transitions are automatic and smooth since the converter operates with a duty cycle of 0.5 at the boundary operation points between the buck and the boost modes, as shown in Figs. 5 and 15.

F. Thermal Analysis of the Prototype

Temperature distributions in the IHMC prototype for the forward and the backward power flow directions under the buck FBI–HBR and the boost FBI–FBR modes are shown in Fig. 18. The highest thermal stress is achieved in the forward and backward power flow directions at $V_{\mathrm{LV}} = 17$ V, $P_{\mathrm{LV}} = 205$ W and $V_{\mathrm{LV}} = 38$ V, $P_{\mathrm{LV}} = 350$ W, respectively. These modes were selected for thermal analysis as the highest stressed

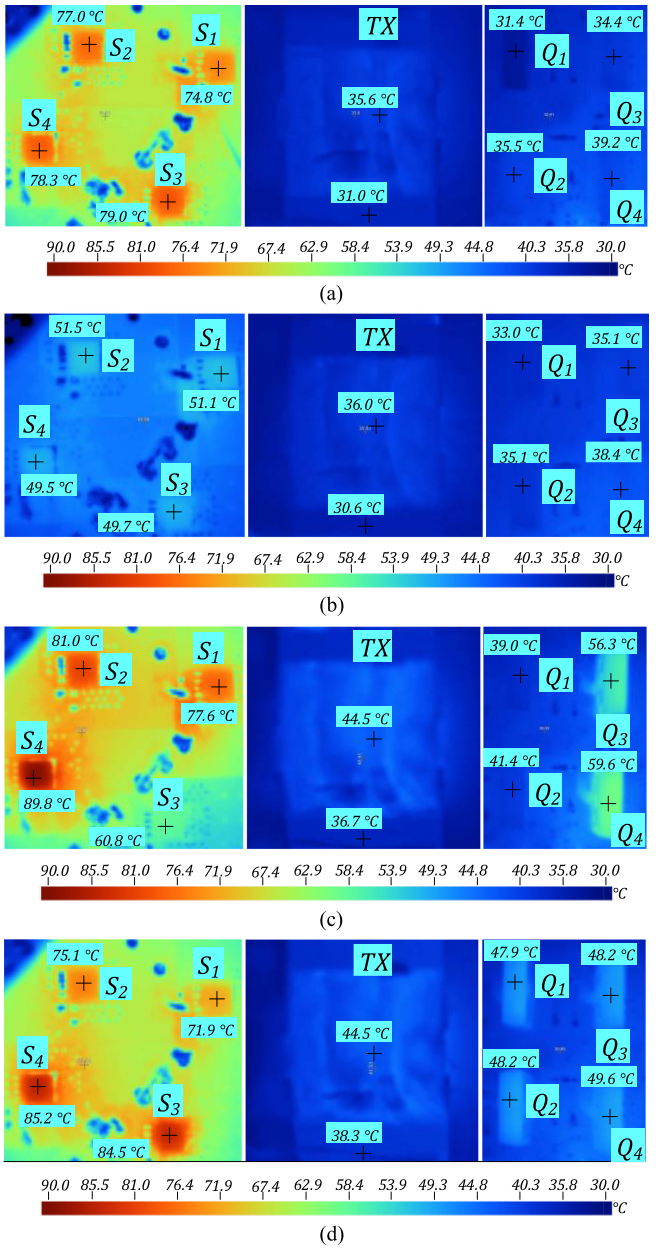

Fig. 18. Temperature distribution in the IHMC in the forward mode under the buck FBI–HBR (a) and the boost FBI–FBI (b) modes at $V_{\mathrm{LV}} = 17$ V and $P_{\mathrm{LV}} = 205$ W and in the backward mode under the buck FBI–HBR (c) and the boost FBI–FBI (d) modes at $V_{\mathrm{LV}} = 38$ V and $P_{\mathrm{LV}} = 350$ W.

modes based on theoretical analysis, which was described in the previous section. Other operating points feature lower thermal stress. The two-times higher secondary-side resonant current and the maximum power in the backward buck FBI–HBR mode are the reasons for the high temperature of the transistors and the transformer, as can be observed from the figures. In the forward buck FBI–HBR mode, the low-voltage switches also have a high temperature, but thermal stress is distributed evenly. However, the core temperature of the transformer in all modes is small because the transformer has been designed for the nominal input voltage $V_{\mathrm{LV}} = 27$ V and the maximum flux density of roughly 90 mT.

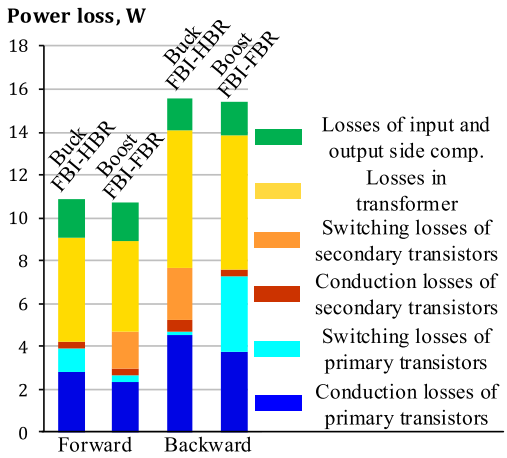

Fig. 19. Power losses in the IHMC under the forward buck FBI–HBR and boost FBI–FBR modes at $V_{\mathrm{LV}} = 17$ V and $P_{\mathrm{LV}} = 205$ W and under the backward buck FBI–HBR and boost FBI–FBR modes at $V_{\mathrm{LV}} = 38$ V and $P_{\mathrm{LV}} = 350$ W.

It follows from the analysis of thermal modes that the proposed IHMC could experience insignificant thermal cycling during the transition between topology configurations. However, these transitions are relatively infrequent (easily ensured by control) as they happen mostly during scanning a source, e.g., during global maximum power point tracking of a PV module. Thus, it could be concluded that they will not threaten the converter's lifetime; passive cooling via printed circuit board surface could be used in the proposed IHMC.

G. Distribution of Power Losses

In order to fully understand the distribution of power losses in the converter in high-stressed operating points, the methodology described in detail in [9] was applied to calculate the conduction losses of primary and secondary transistors (blue and brown), switching losses of primary and secondary transistors (light blue and orange), conduction losses of the transformer windings (yellow), and combined losses of the input- and output-side components (green) in the buck FBI–HBR and boost FBI–HBR control modes at $V_{\mathrm{LV}} = 17$ V and $P_{\mathrm{LV}} = 208$ W in the forward direction and at $V_{\mathrm{LV}} = 38$ V and $P_{\mathrm{LV}} = 350$ W in the backward direction (see Fig. 19). The calculated power loss breakdowns correlate with the experimental results and the temperature of the components in both converters. The conduction losses of the low-voltage side switches and conduction and switching losses of the high-voltage side switches are the highest in the backward buck FBI–HBR mode. The switching losses of the low-voltage side switches are the highest in the backward boost FBI–FBR mode. These observations prompt the conclusion that total losses of the converter are higher in the backward direction. Therefore, this aspect should be taken into account in the thermal design of the IHMC.

V. Conclusion

In this article, the bidirectional isolated hexamode dc–dc converter is proposed for wide gain range applications in dc microgrids. Thanks to the TMC based on the hybrid switching cells, the converter operates under six control modes in both directions. The operating principles and theoretical equations for the calculation of the dc voltage gains and the duty cycle of each mode are described. Compared to conventional two-mode buck–boost converters, the proposed converter avoids any abnormal operation by keeping the converter buck or boost factor below twofold.

A 350-W rated prototype with a low-voltage range from 10 up to 60 V and a 350 V output voltage was built to be compatible with typical residential PV modules and batteries. It was demonstrated that the converter can keep the efficiency above 94% in the forward direction by harnessing the high efficiencies of three DCX operating points. This remarkable result was achieved despite converter operation at the SOA envelope, i.e., maximum power/current. The peak efficiency of the built prototype achieved is 98.1% in the forward direction and 97.6% in the backward direction. The proposed converter achieves the high-efficiency zero-voltage switching and/or zero-current switching of the input and output side switches. It should be noted that the converter operates under a fixed switching frequency, and only one or two switches are turned OFF with high current in each of the six operating modes.

Appendix

Expressions for the calculation of switching and rms current in the converter under the buck FBI–HBR mode in any direction are derived below.

The amplitude of the resonant current during the active state can be defined as follows:

$$I_{\mathrm{lk1}} = \frac{V_{\mathrm{in}} \cdot n + \frac{V_{\mathrm{out}}}{2} - \frac{\Delta V_{Cr}}{2}}{Z_r} \tag{33}$$

where Z_r is the impedance of the resonant tank and ΔV_{Cr} is the peak-to-peak voltage ripple of the equivalent resonant capacitor C_r, which are given as follows:

$$Z_r = \sqrt{\frac{L_{\mathrm{lk}}}{C_r}} \tag{34}$$

$$\Delta V_{Cr} = \frac{I_{\mathrm{out}}}{C_r \cdot f_S} \tag{35}$$

$$C_r = \frac{C_2 \cdot C_3}{C_2 + C_3 \cdot n^2}. \tag{36}$$

The peak of the magnetizing current equals

$$I_{Lm(\max)} = \frac{V_{\mathrm{in}} \cdot n \cdot D_{\mathrm{bk}}}{2 \cdot L_m \cdot f_{\mathrm{SW}}}. \tag{37}$$

Therefore, the switching current of primary-side lagging-leg transistors can be calculated as follows:

$$I_{\mathrm{in,tr(SW)}} = n \cdot \left(I_{\mathrm{lk1}} \cdot \sin\left(D_{\mathrm{bk}} \cdot T_{\mathrm{SW}} \cdot \omega_r\right) + I_{Lm(\max)}\right). \tag{38}$$

The voltage of the equivalent resonant capacitor C_r at the end of the active state equals

$$V_{Cr(D)} = I_{\mathrm{lk1}} \cdot Z_r \cdot \cos(D_{\mathrm{bk}} \cdot T_{\mathrm{SW}} \cdot \omega_r) - V_{\mathrm{in}} \cdot n. \tag{39}$$

The amplitude of the resonant current during the falling state can be calculated as follows:

$$I_{\text{lk2}} = \sqrt{\left(I_{\text{lk1}} \cdot \sin\left(D_{\text{bk}} \cdot T_{\text{SW}} \cdot \omega_r\right)\right)^2 + \left(\frac{V_{Cr(D)}}{Z_r}\right)^2}. \quad (40)$$

Period of falling the resonant current equals

$$\Delta t_f = \frac{1}{\omega_r} \arcsin\left(\frac{I_{\text{lk1}} \cdot \sin\left(\omega_r \cdot D_{\text{bk}} \cdot T_{\text{SW}}\right)}{I_{\text{lk2}}}\right). \quad (41)$$

For simplifying the following description, three equation are taken

$$O_1 = {I_{\text{lk1}}}^2 \left(D_{\text{bk}} \cdot T_{\text{SW}} \cdot \omega_r - \cos\left(D_{\text{bk}} \cdot T_{\text{SW}} \cdot \omega_r\right) \times \sin\left(D_{\text{bk}} \cdot T_{\text{SW}} \cdot \omega_r\right)\right) \quad (42)$$

$$O_2 = {I_{\text{lk2}}}^2 \left(\cos\left(\Delta t_f \cdot \omega_r\right) \cdot \sin\left(\Delta t_f \cdot \omega_r\right) + \Delta t_f \cdot \omega_r\right) \quad (43)$$

$$O_3 = \frac{f_{\text{SW}}}{2 \cdot \omega_r}\left(O_1 + O_2\right). \quad (44)$$

The rms currents of the transformer primary and secondary windings equal

$$I_{\text{TX,pr(RMS)}} = n \cdot \sqrt{2 \cdot O_3 + 2 \cdot {I_{Lm(\max)}}^2 \cdot \left(\Delta t_f \cdot f_{\text{SW}} + \frac{D_{\text{bk}}}{3}\right)} \quad (45)$$

$$I_{\text{TX,sec(RMS)}} = \sqrt{2 \cdot O_3 + 2 \cdot {I_{Lm(\max)}}^2 \cdot \frac{\Delta t_2 \cdot f_{\text{SW}}}{3}} \quad (46)$$

where $\Delta t_2 = 1 - \Delta t_f - D_{\text{bk}} \cdot T_{\text{SW}}$.

The rms current of primary-side switches equals

$$I_{\text{in,tr(RMS)}} = n \cdot \sqrt{O_3 + {I_{Lm(\max)}}^2 \cdot \left(\Delta t_f \cdot f_{\text{SW}} + \frac{D_{\text{bk}}}{3}\right)}. \quad (47)$$

The rms current of output-side switches (Q_1 and Q_2) equals

$$I_{\text{out,tr}_{1,2}\text{(RMS)}} = \sqrt{O_3 + {I_{Lm(\max)}}^2 \cdot \frac{\Delta t_2 \cdot f_{\text{SW}}}{3}}. \quad (48)$$

The rms current of the output-side switch (Q_4) equals

$$I_{\text{out,tr}_4\text{(RMS)}} = I_{\text{TX,sec(RMS)}}. \quad (49)$$

The rms current of the output-side filter capacitor (C_4) also equals to the rms current of transformer secondary windings

$$I_{\text{out},C_4\text{(RMS)}} = I_{\text{TX,sec(RMS)}}. \quad (50)$$

The rms current of the input filter capacitor (C_1) equals

$$I_{\text{in},C_1\text{(RMS)}} = n \cdot \sqrt{\frac{f_{\text{SW}}}{\omega_r} O_1}. \quad (51)$$

REFERENCES

[1] E. Rodriguez-Diaz, J. C. Vasquez, and J. M. Guerrero, "Intelligent DC homes in future sustainable energy systems: When efficiency and intelligence work together," *IEEE Consum. Electron. Mag.*, vol. 5, no. 1, pp. 74–80, Jan. 2016.

[2] M. Forouzesh, Y. P. Siwakoti, S. A. Gorji, F. Blaabjerg, and B. Lehman, "Step-up DC–DC converters: A comprehensive review of voltage-boosting techniques, topologies, and applications," *IEEE Trans. Power Electron.*, vol. 32, no. 12, pp. 9143–9178, Dec. 2017.

[3] O. Matiushkin, O. Husev, J. Rodriguez, H. Young, and I. Roasto, "Feasibility study of model predictive control for grid-connected twisted buck–boost inverter," *IEEE Trans. Ind. Electron.*, vol. 69, no. 3, pp. 2488–2499, Mar. 2022.

[4] S. Kouro, J. I. Leon, D. Vinnikov, and L. G. Franquelo, "Grid-connected photovoltaic systems: An overview of recent research and emerging PV converter technology," *IEEE Ind. Electron. Mag.*, vol. 9, no. 1, pp. 47–61, Mar. 2015.

[5] C. Yao, X. Ruan, X. Wang, and C. K. Tse, "Isolated buck–boost DC/DC converters suitable for wide input-voltage range," *IEEE Trans. Power Electron.*, vol. 26, no. 9, pp. 2599–2613, Sep. 2011.

[6] Y. Lu, H. Wu, K. Sun, and Y. Xing, "A family of isolated buck–boost converters based on semiactive rectifiers for high-output voltage applications," *IEEE Trans. Power Electron.*, vol. 31, no. 9, pp. 6327–6340, Sep. 2016.

[7] A. Chub, D. Vinnikov, R. Kosenko, and E. Liivik, "Wide input voltage range photovoltaic microconverter with reconfigurable buck–boost switching stage," *IEEE Trans. Ind. Electron.*, vol. 64, no. 7, pp. 5974–5983, Jul. 2017.

[8] T. LaBella, W. Yu, J. Lai, M. Senesky, and D. Anderson, "A bidirectional-switch-based wide-input range high-efficiency isolated resonant converter for photovoltaic applications," *IEEE Trans. Power Electron.*, vol. 29, no. 7, pp. 3473–3484, Jul. 2014.

[9] V. Sidorov, A. Chub, D. Vinnikov, and A. Bakeer, "An overview and comprehensive comparative evaluation of constant-frequency voltage buck control methods for series resonant DC–DC converters," *IEEE Open J. Ind. Electron. Soc.*, vol. 2, pp. 65–79, 2021.

[10] A. Chub, D. Vinnikov, and J. Lai, "Input voltage range extension methods in the series-resonant DC–DC converters," in *Proc. IEEE 15th Brazillian Power Electron. Conf./5th IEEE Southern Power Electron. Conf.*, 2019, pp. 1–6.

[11] J.-P. Vandelac and P. D. Ziogas, "A DC to DC PWM series resonant converter operated at resonant frequency," *IEEE Trans. Ind. Electron.*, vol. 35, no. 3, pp. 451–460, Aug. 1988.

[12] X. Zhao, C. Chen, and J. Lai, "A high-efficiency active-boost-rectifier-based converter with a novel double-pulse duty cycle modulation for PV to DC microgrid applications," *IEEE Trans. Power Electron.*, vol. 34, no. 8, pp. 7462–7473, Aug. 2019.

[13] J. Hassan, C. Bai, J. -W. Lim, and M. Kim, "High step-up quasi-resonant converter featuring minimized switching loss over wide input voltage range," *IEEE Trans. Ind. Electron.*, vol. 68, no. 11, pp. 10784–10795, Nov. 2021.

[14] J. Hassan, C. Bai, H. Seok, J. -W. Lim, S. -H. Ahn, and M. Kim, "Highly efficient current-fed half-bridge resonant converter for pulse power applications," *IEEE Trans. Power Electron.*, vol. 37, no. 3, pp. 3192–3204, Mar. 2022.

[15] N. -G. Kim, B. Han, S. -W. Jo, and M. Kim, "High-voltage-gain soft-switching converter employing bidirectional switch for fuel-cell vehicles," *IEEE Trans. Veh. Technol.*, vol. 70, no. 9, pp. 8731–8743, Sep. 2021.

[16] J. -W. Lim, J. Hassan, and M. Kim, "Bidirectional soft switching push–pull resonant converter over wide range of battery voltages," *IEEE Trans. Power Electron.*, vol. 36, no. 11, pp. 12251–12267, Nov. 2021.

[17] A. Bakeer, A. Chub, A. Blinov, and J.-S. Lai, "Wide range series resonant DC–DC converter with a reduced component count and capacitor voltage stress for distributed generation," *Energies*, vol. 14, no. 8, Apr. 2021, Art. no. 2051.

[18] J. Kim, M. Park, J. Han, M. Lee, and J. Lai, "PWM resonant converter with asymmetric modulation for ZVS active voltage doubler rectifier and forced half resonance in PV application," *IEEE Trans. Power Electron.*, vol. 35, no. 1, pp. 508–521, Jan. 2020.

[19] X. Zhao, L. Zhang, R. Born, and J. Lai, "A high-efficiency hybrid resonant converter with wide-input regulation for photovoltaic applications," *IEEE Trans. Ind. Electron.*, vol. 64, no. 5, pp. 3684–3695, May 2017.

[20] J.-W. Kim and P. Barbosa, "PWM-controlled series resonant converter for universal electric vehicle charger," *IEEE Trans. Power Electron.*, vol. 36, no. 12, pp. 13578–13588, Dec. 2021.

[21] A. Bakeer, A. Chub, and D. Vinnikov, "Series resonant DC–DC converter with single-switch full-bridge boost rectifier operating at fixed switching frequency," in *Proc. IEEE 11th Int. Symp. Power Electron. Distrib. Gener. Syst.*, 2020, pp. 270–275.

[22] J. Kim, S. -W. Ryu, M. Kim, and J. -W. Jung, "Triple-mode isolated resonant buck–boost converter over wide input voltage range for residential applications," *IEEE Trans. Ind. Electron.*, vol. 68, no. 11, pp. 11087–11099, Nov. 2021.
[23] V. Sidorov, A. Chub, and D. Vinnikov, "Efficiency improvement of step-up series resonant DC–DC converter in buck operating mode," in *Proc. IEEE 61st Int. Sci. Conf. Power Elect. Eng. Riga Tech. Univ.*, 2020, pp. 1–6.
[24] A. Bakeer, A. Chub, D. Vinnikov, and A. Rosin, "Wide input voltage range operation of the series resonant DC–DC converter with bridgeless boost rectifier," *Energies*, vol. 13, no. 16, Aug. 2020, Art. no. 4220.
[25] V. Sidorov, A. Chub, and D. Vinnikov, "Topology morphing control with soft transients for multimode series resonant DC–DC converter," in *Proc. IEEE 22nd Int. Conf. Young Professionals Electron Devices Mater.*, 2021, pp. 331–336.
[26] V. Sidorov, A. Chub, and D. Vinnikov, "Accelerated global MPPT for multimode series resonant DC–DC converter," in *Proc. IEEE 15th Int. Conf. Compat., Power Electron. Power Eng.*, 2021, pp. 1–6.
[27] S. Rahman, V. Sidorov, A. Chub, and D. Vinnikov, "High frequency split-bobbin transformer design with adjustable leakage inductance," in *Proc. IEEE 62nd Int. Sci. Conf. Power Elect. Eng. Riga Tech. Univ.*, 2021, pp. 1–5.

Vadim Sidorov (Student Member, IEEE) was born in Kazakhstan in 1995. He received the B.Sc. and M.Sc. degrees in power electronics from Novosibirsk State Technical University, Novosibirsk, Russia, in 2017 and 2019, respectively. He is currently working toward the Ph.D. degree in the power electronics Group, Tallinn University of Technology, Tallinn, Estonia.

He has coauthored more than 20 papers and 1 book chapter on power electronics and applications. His research interests include power electronics systems, dc–dc converters, series resonant converters, dc–ac inverters, and electric drive systems.

Andrii Chub (Senior Member, IEEE) received the B.Sc. and M.Sc. degrees in electronic systems from the Chernihiv State Technological University, Chernihiv, Ukraine, in 2008 and 2009, respectively, and the Ph.D. degree in electrical engineering from the Tallinn University of Technology, Tallinn, Estonia, in 2016.

He is currently a Senior Researcher with Power Electronics Group, Department of Electrical Power Engineering and Mechatronics, Tallinn University of Technology. He was a Visiting Research Fellow with Kiel University in 2017 and a Postdoctoral Researcher with Federico Santa Maria Technical University between 2018 and 2019. He has coauthored more than 100 papers and a book chapter on power electronics and applications. He holds several patents and utility models. His research interests include advanced dc–dc converter topologies, renewable energy conversion systems, energy-efficient buildings, and reliability and fault tolerance of power electronic converters.

Dr. Chub is an Associate Editor for the IEEE JOURNAL OF EMERGING AND SELECTED TOPICS IN INDUSTRIAL ELECTRONICS. He received numerous best paper awards at IEEE conferences and the 2018 IEEE Industrial Electronics Society Best Conference Paper Award.

Dmitri Vinnikov (Senior Member, IEEE) received the Dipl.Eng., M.Sc., and Dr.Sc.Techn. degrees in electrical engineering from the Tallinn University of Technology, Tallinn, Estonia, in 1999, 2001, and 2005, respectively.

He is currently the Head of the Power Electronics Group, Department of Electrical Power Engineering and Mechatronics, Tallinn University of Technology. He is the Head of R&D and cofounder of Ubik Solutions LLC—Estonian start-up company dedicated to innovative and smart power electronics for renewable energy systems. Moreover, he is one of the founders and leading researchers of ZEBE—Estonian Centre of Excellence for Zero Energy and Resource Efficient Smart Buildings and Districts. He has authored or coauthored 2 books, 5 monographs, and 1 book chapter, as well as more than 400 published papers on power converter design and development. He holds numerous patents and utility models in this field. His research interests include applied design of power electronic converters and control systems, renewable energy conversion systems (photovoltaic and wind), impedance-source power converters, and implementation of wide-bandgap power semiconductors.

Dr. Vinnikov is the Chair of the IEEE Estonia Section.